catalysts

MDPI

Article

Fe-Modified Mesh-Structured Mn_2O_3/γ-Al_2O_3/Al Catalysts: Enriched Surface Active Oxygen and Superior Redox Properties for Enhanced NH_3-SCO Performance

Jingling Pei [1], Qingli Shu [1], Wenwen Zhang [1] and Qi Zhang [1,2,*]

[1] School of Chemical Engineering, East China University of Science and Technology, Shanghai 200237, China; y82230027@mail.ecust.edu.cn (J.P.); y20210022@mail.ecust.edu.cn (Q.S.); y21220004@mail.ecust.edu.cn (W.Z.)
[2] State Key Laboratory of Green Chemical Engineering and Industrial Catalysis, School of Chemical Engineering, East China University of Science and Technology, Shanghai 200237, China
* Correspondence: zhangqi@ecust.edu.cn

Abstract

Ammonia-selective catalytic oxidation (NH_3-SCO) is an effective technology for eliminating NH_3 slip; however, the development of catalysts that simultaneously exhibit excellent low-temperature (<350 °C) activity and high N_2 selectivity remains a significant challenge. A novel structured monolithic mesh-type Fe_x-Mn_2O_3/γ-Al_2O_3/Al catalyst was developed. XPS, H_2-TPR, and O_2-TPD results demonstrate that Fe doping markedly increases the concentration of surface-adsorbed active oxygen species and enhances the redox capability. As a result, the optimally doped $Fe_{6.61}$-Mn_2O_3/γ-Al_2O_3/Al catalyst achieved complete NH_3 conversion at 210 °C with a 75% N_2 selectivity, outperforming previously reported Mn-based catalysts. Density functional theory (DFT) calculations further confirm that Fe modification enhances O_2 adsorption energy. In addition, the introduction of Fe significantly improves the catalyst's resistance to SO_2 and H_2O. In situ FTIR results indicate that the NH_3-SCO reaction over Fe-Mn_2O_3/γ-Al_2O_3/Al proceeds predominantly via an internal selective catalytic reduction (i-SCR) pathway.

Keywords: NH_3-SCO; Mn_2O_3; Fe-doped; monolithic support; surface active oxygen

1. Introduction

Atmospheric pollution and its health risks have long been a concern in environmental science and public health. Recently, ammonia (NH_3) emissions, primarily from fertilizer use, industrial processes, and NH_3-SCR NO_x abatement [1,2], have garnered increased attention. NH_3 exposure can irritate the respiratory system, skin, and eyes, and may impair tissue functions [3]. Therefore, effective control of NH_3 emissions is crucial for improving air quality.

Among various NH_3 removal methods developed previously, ammonia-selective catalytic oxidation (NH_3-SCO) has attracted extensive attention in recent years because it can directly convert NH_3 into environmentally benign N_2 and H_2O [4] and is regarded as the most promising technology for NH_3 degradation. Noble metal catalysts such as Au and Pt exhibit the highest low-temperature activity in NH_3-SCO [5], but their low N_2 selectivity and high cost limit their large-scale application [6,7]. Therefore, great efforts have been devoted to exploring low-cost NH_3-SCO catalysts, and manganese oxides have recently been considered promising NH_3-SCO catalysts. Previous studies have shown that the crystal phase of MnO_x is crucial for the catalyst's selectivity. Qu et al. [8] synthesized MnO_2

Academic Editor: Piotr Kuśtrowski

Received: 24 February 2026
Revised: 18 March 2026
Accepted: 25 May 2026
Published: 26 June 2026

(UH), which achieved 100% NH_3 conversion at 170 °C, but its N_2 selectivity was only 49%. The Mn_2O_3 phase exhibits the highest N_2 selectivity in the NH_3-SCR reaction, but its low-temperature activity is relatively poor [9]. Therefore, achieving the coexistence of high conversion and high selectivity at low temperature (<350 °C [10]) remains a key challenge for Mn-based catalysts. In this context, doping modification has been recognized as an effective strategy for optimizing the catalytic performance of MnO_x. Madhuri et al. [11] demonstrated that Fe_2O_3 doping of Mn_2O_3 significantly increased the surface-adsorbed oxygen concentration, enhancing catalytic activity without affecting benzonitrile selectivity. Similarly, Yu et al. [12] reported that the $Mn_{1.82}Fe_{0.18}O_3$ catalyst, formed by Fe incorporation into Mn_2O_3, exhibited excellent performance in toluene oxidation, attributed to increased surface acid site density and higher active oxygen concentration due to Fe doping. These studies indicate that Fe modification of Mn_2O_3 improves its low-temperature oxidation performance. These findings provide new insights for enhancing NH_3 conversion in Mn_2O_3 catalysts through Fe doping and achieving a balance between high activity and high N_2 selectivity.

On the other hand, traditional granular or powder catalysts suffer from issues such as poor mechanical strength, high pressure drop, limited mass transfer, and particle loss [13,14], which restrict their long-term stable operation. While monolithic catalysts alleviate some of these problems, their washcoating method leads to weak interactions between the active components and the support, affecting the catalyst's long-term stability and activity. To overcome these shortcomings, a mesh-structured γ-Al_2O_3/Al support, prepared by anodization, was proposed in our previous work and applied for the removal of pollutants such as O_3, HCHO, and CO [15–19]. This support features excellent mechanical properties and a three-dimensional interconnected pore structure [20], effectively enhancing mass and heat transfer [21]. However, there are few reports on the application of these anodized, in situ-grown monolithic catalysts in NH_3-SCO reactions.

In this study, a novel structured monolithic mesh Fe_x-Mn_2O_3/γ-Al_2O_3/Al catalyst was developed for low-temperature selective catalytic oxidation of NH_3 (NH_3-SCO). First, a series of characterizations were conducted to systematically reveal the effects of Fe doping on surface active adsorbed oxygen species and redox properties of the Mn_2O_3/γ-Al_2O_3/Al catalyst. Density functional theory (DFT) calculations were further performed to analyze the influence of Fe doping on the O_2 adsorption energy on the catalyst surface. In addition, water and sulfur resistance evaluations were carried out to assess the role of Fe species in the reaction system. Finally, the evolution of key surface intermediates was tracked by in situ Fourier transform infrared spectroscopy (in situ FTIR), based on which a possible NH_3-SCO reaction mechanism was proposed.

2. Results and Discussion

2.1. The Effect of Mn Crystal Phases on NH_3-SCO Performance over a γ-Al_2O_3/Al Carrier

Figure 1a–c present the SEM images of the AAO/Al and γ-Al_2O_3/Al supports obtained after anodization and subsequent treatments of the Al substrate. As shown in Figure 1a, a typical "sandwich" structure is formed after anodization, where anodic alumina layers with a thickness of approximately 90 μm are in situ grown on both sides of the Al substrate. The in situ-grown Al_2O_3 layers are tightly bonded to the metallic Al substrate, which effectively suppresses the detachment of active coatings commonly observed in conventional washcoated supports under harsh conditions such as high temperature, high humidity, or high gas velocity, thereby enhancing the structural stability of the monolithic catalyst. As shown in Figure 1b, the AAO precursor exhibits a highly ordered and uniform nanochannel structure with a relatively narrow pore size distribution and a smooth surface. After thermal treatment, the AAO precursor is successfully transformed into γ-Al_2O_3/Al,

accompanied by pronounced morphological changes (Figure 1c). Compared with the AAO precursor, γ-Al_2O_3/Al shows a much rougher surface, where the ordered nanochannels evolve into a honeycomb-like porous network with wrinkled and irregular pore walls [17]. Such a porous structure provides abundant anchoring sites for the deposition of active phases, thereby strengthening the interaction between the active species and the support.

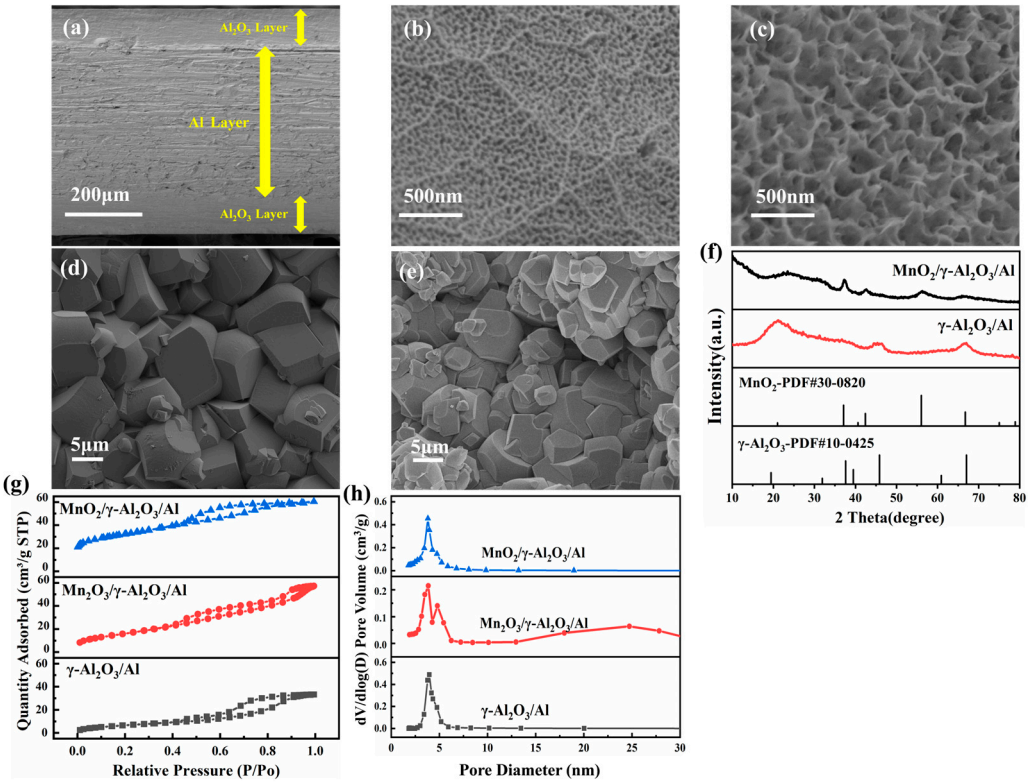

Figure 1. SEM images of cross-section of AAO/Al (**a**), AAO/Al (**b**), γ-Al_2O_3/Al (**c**), MnO_2/γ-Al_2O_3/Al (**d**), Mn_2O_3/γ-Al_2O_3/Al (**e**); XRD patterns (**f**), N_2 adsorption/desorption isotherms (**g**) and pore size distributions (**h**) of γ-Al_2O_3/Al, MnO_2/γ-Al_2O_3/Al, and Mn_2O_3/γ-Al_2O_3/Al.

As shown in Figure 1d,e, Mn species supported on γ-Al_2O_3/Al lead to MnO_2/γ-Al_2O_3/Al and Mn_2O_3/γ-Al_2O_3/Al catalysts exhibiting polyhedral morphologies. The XRD patterns (Figure 1f) confirm the successful formation of γ-Al_2O_3, MnO_2/γ-Al_2O_3/Al. In addition, our previous study demonstrated that γ-Al_2O_3/Al possesses a high density of Lewis acid sites [22], which is favorable for the stable anchoring of Mn species as well as for NH_3 adsorption.

As shown in Figure 1g, all samples exhibit typical type IV adsorption–desorption isotherms with distinct H3 hysteresis loops, indicating the predominance of mesoporous structures. The H3-type hysteresis loop is generally associated with slit-shaped pores formed by the aggregation of plate-like particles [23]. The corresponding pore size distribution (Figure 1h) reveals that the dominant pore sizes are centered at 3–4 nm. Combined with the honeycomb-like morphology observed by SEM, these results suggest that a mesoporous network structure is formed during the thermal transformation from AAO/Al to γ-Al_2O_3/Al through pore wall stacking and channel reconstruction. As a result, the specific surface area of γ-Al_2O_3/Al increases significantly from 11 to 102 $m^2 \cdot g^{-1}$, which contributes to improved dispersion of active species. After loading Mn species onto γ-Al_2O_3/Al, the specific surface area further increases from 89 to 140–145 $m^2 \cdot g^{-1}$ (Table 1), which is conducive to the exposure of active sites relevant to the NH_3-SCO reaction.

Table 1. Textural properties and Mn loading of AAO, γ-Al_2O_3/Al, MnO_2/γ-Al_2O_3/Al, and Mn_2O_3/γ-Al_2O_3/Al.

Catalysts	S_{BET} [a]/$m^2 \cdot g^{-1}$	V_{pore} [b]/$cm^3 \cdot g^{-1}$	D_p [b]/nm	Mn [c]/wt%
AAO	11	0.13	34.72	0
γ-Al_2O_3/Al	102	0.15	4.22	0
MnO_2/γ-Al_2O_3/Al	145	0.19	3.59	17.3
Mn_2O_3/γ-Al_2O_3/Al	140	0.16	4.55	17.1

[a] From the isotherm analysis in the P/P_0 range of 0.04~0.12; [b] from the desorption curve of the BJH method; [c] Mn/wt% and Fe/wt% were measured by the ICP-AES.

In this study, the novel mesh γ-Al_2O_3/Al support was employed in the development of the optimal crystalline phase and Fe-modified Mn-based catalysts for the NH_3-SCO reaction. Figure 2 presents a comparison of the catalytic performance of MnO_2/γ-Al_2O_3/Al and Mn_2O_3/γ-Al_2O_3/Al in this reaction. In the 100–240 °C range, a higher NH_3 conversion rate was achieved by MnO_2/γ-Al_2O_3/Al compared to Mn_2O_3/γ-Al_2O_3/Al, with a T_{100} (the temperature at which NH_3 conversion reaches 100%) of 200 °C, which is 240 °C lower than that of Mn_2O_3/γ-Al_2O_3/Al (Figure 2a). However, much lower N_2 selectivity was observed for MnO_2/γ-Al_2O_3/Al, with a N_2 selectivity of only 50% at T_{100}, while over 80% was achieved by Mn_2O_3/γ-Al_2O_3/Al (Figure 2b). As shown in Figure 2c, although the NH_3 conversion of Mn_2O_3/γ-Al_2O_3/Al was lower at low temperatures, a significantly higher N_2 yield was obtained, demonstrating superior de-ammoniation performance.

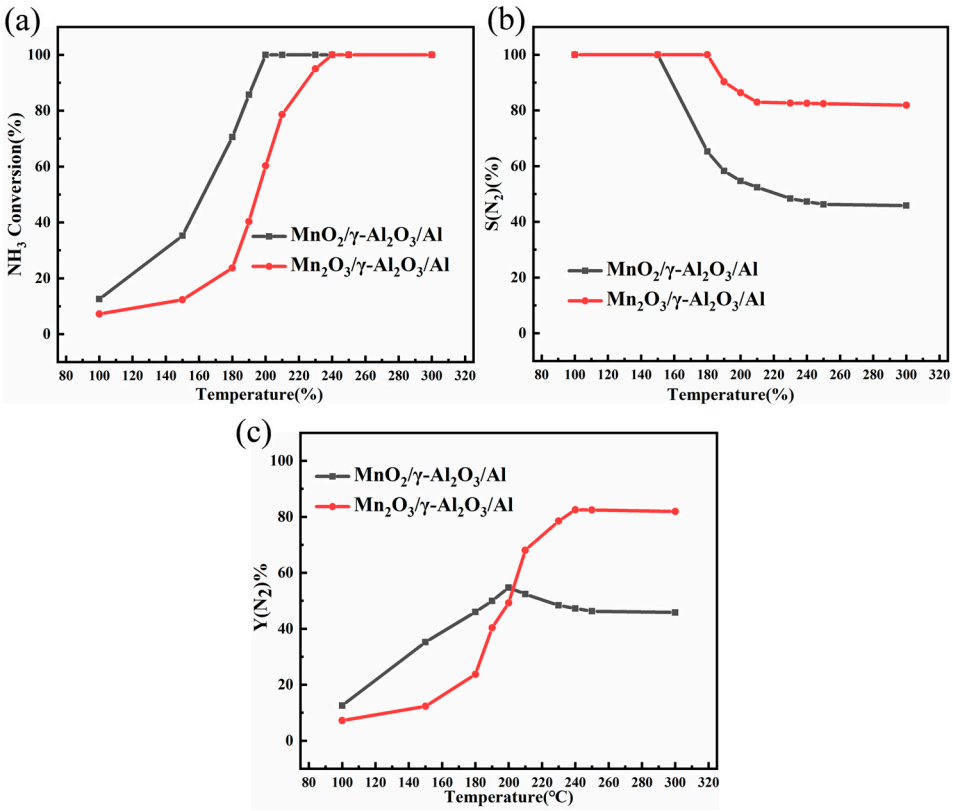

Figure 2. NH_3 conversion (**a**), N_2 selectivity (**b**), N_2 yield of MnO_2/γ-Al_2O_3/Al and Mn_2O_3/γ-Al_2O_3/Al catalysts (**c**) (reaction conditions: $[NH_3]$ = 3000 ppm; WHSV = 25,000 $mL \cdot g_{cat}^{-1} \cdot h^{-1}$).

2.2. Effect of Fe Modification on NH_3-SCO Activity over Fe_x-Mn_2O_3/γ-Al_2O_3/Al Catalysts

It has been reported that Fe incorporation into Mn_2O_3 catalysts modifies the surface electronic structure and redox properties in VOC catalytic oxidation systems. In particular, Fe doping has been shown to increase the proportion of surface-adsorbed oxygen species

and enhance the density of acid sites [11,12], thereby facilitating oxidation reactions. Based on these considerations, Fe was introduced into the $Mn_2O_3/\gamma\text{-}Al_2O_3/Al$ catalyst in this work, and its structural and physicochemical properties were first investigated before evaluating the NH_3-SCO performance.

N_2 adsorption–desorption experiments were conducted to investigate the textural properties of the catalysts. As shown in Figure 3a, all catalysts exhibited BET Type IV isotherms [24], with an H3-type hysteresis loop in the p/p_0 = 0.4–1 range, indicating a predominant slit-like mesoporous structure. The pore size distribution (Figure 3b) reveals that the majority of the pores are concentrated in the 4–5 nm range. According to the data in Tables 1 and 2, Fe doping leads to noticeable changes in the textural properties of the catalysts: the specific surface area of $Fe_{6.61}\text{-}Mn_2O_3/\gamma\text{-}Al_2O_3/Al$ increased from 140 m^2/g to 175 m^2/g, the pore volume rose from 0.16 cm^3/g to 0.23 cm^3/g, and the average pore size increased from 4.55 nm to 5.81 nm. Notably, when the Fe loading exceeded 8.32 wt%, both the specific surface area and pore volume slightly decreased, indicating the presence of an optimal doping amount, which is consistent with the observed catalytic activity.

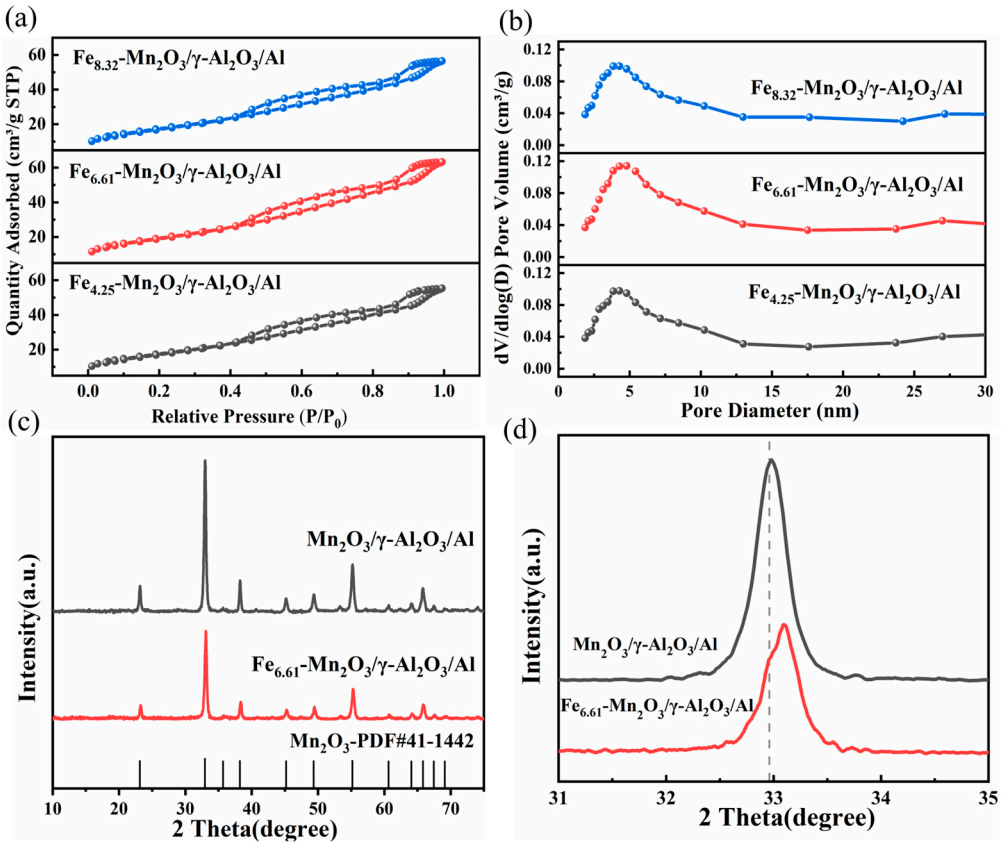

Figure 3. N_2 adsorption–desorption isotherms (**a**) and pore size distribution curves (**b**) of $Fe_x\text{-}Mn_2O_3/\gamma\text{-}Al_2O_3/Al$ (x = 4.25, 6.61 and 8.32) catalysts; XRD patterns of $Mn_2O_3/\gamma\text{-}Al_2O_3/Al$ and $Fe_{6.61}\text{-}Mn_2O_3/\gamma\text{-}Al_2O_3/Al$ (**c**) (magnified XRD patterns of $Mn_2O_3/\gamma\text{-}Al_2O_3/Al$ and $Fe_{6.61}\text{-}Mn_2O_3/\gamma\text{-}Al_2O_3/Al$ (**d**)).

Figure 3c,d display the XRD patterns of the catalysts. Diffraction peaks corresponding to the (211), (222), (400), (332), (431), and (440) planes of cubic Mn_2O_3 are observed at 2θ = 23.131°, 32.951°, 38.234°, 45.178°, 49.347°, and 55.189°, respectively. No impurity peaks associated with Fe_2O_3 or spinel structures were observed, suggesting that Fe atoms substituted Mn atoms in the lattice through isomorphous substitution, successfully forming a single-phase Mn_2O_3 [25]. Additionally, the magnified XRD pattern (Figure 3d) reveals a noticeable shift of the (222) peak towards higher diffraction angles with Fe doping.

According to the Bragg equation, the lattice constants (a) for Mn_2O_3 and $Fe_{6.61}$-Mn_2O_3 are 9.401 Å and 9.380 Å, respectively, confirming a contraction of the unit cell. This is mainly attributed to the smaller ionic radius of Fe compared to Mn [26], indicating that Fe atoms are incorporated into the Mn_2O_3 lattice, forming a single-phase Fe-Mn mixed oxide.

Table 2. Textural properties and Fe/Mn loadings of Fe_x-Mn_2O_3/γ-Al_2O_3/Al catalysts (x = 4.25, 6.61, and 8.32).

Catalysts	S_{BET} [a]/$m^2 \cdot g^{-1}$	V_{pore} [b]/$cm^3 \cdot g^{-1}$	D_p [b]/nm	Mn [c]/wt%	Fe [c]/wt%
$Fe_{4.25}$-Mn_2O_3/γ-Al_2O_3/Al	159	0.20	5.59	17.1	4.25
$Fe_{6.61}$-Mn_2O_3/γ-Al_2O_3/Al	175	0.23	5.81	17.4	6.61
$Fe_{8.32}$-Mn_2O_3/γ-Al_2O_3/Al	167	0.21	5.60	17.3	8.32

[a] From the isotherm analysis in the P/P_0 range of 0.04~0.12; [b] from the desorption curve of the BJH method; [c] Mn/wt% and Fe/wt% were measured by ICP-AES.

SEM images reveal that the Fe doping amount markedly affects the particle morphology and packing of Mn_2O_3. The undoped Mn_2O_3/γ-Al_2O_3/Al (Figure 4a) mainly consists of regular polyhedral particles with a broad size distribution of 5–8 μm. The particle surfaces are smooth, the crystal planes are well-defined, and the particles are densely packed, indicative of high crystallinity. Upon Fe introduction, $Fe_{4.25}$-Mn_2O_3/γ-Al_2O_3/Al (Figure 4b) retains the polyhedral morphology, although the particle size slightly decreases, and surface features such as steps and edges emerge. The particles become more loosely packed. With a further increase in Fe doping to 6.61 wt% (Figure 4c), the particle size distribution becomes more uniform, grain size decreases further, and surface steps and crystal boundaries are more prominently exposed. This observation is consistent with the highest specific surface area observed for this sample. A larger specific surface area is beneficial for the adsorption of reactants. Wei et al. [27] analyzed unmodified 13X zeolite and Mn-Fe/13X catalysts using SEM and found that the formation of cubic structures and petal-like layered MnO_2 on the surface contributed to an increased specific surface area, thereby enhancing ozone adsorption. Furthermore, no significant large-scale agglomeration is observed for the $Fe_{6.61}$-Mn_2O_3/γ-Al_2O_3/Al catalyst, indicating good dispersion of the active species. It has been reported that good dispersion can enhance catalytic activity. For instance, Wen et al. [28] reported that the active components in Mn-Fe-Ce/Al_2O_3/CC catalysts exhibited better dispersion than those in Mn-Fe-Ce/CC samples, which was considered one of the main reasons for the improved catalytic activity. When the Fe content reaches 8.32 wt% (Figure 4d), partial particle agglomeration occurs, with small particles adhering to larger ones to form dense secondary stacking structures. Particle boundaries appear blurred, which may limit the full exposure of active surface sites. This observation is in agreement with the above discussion.

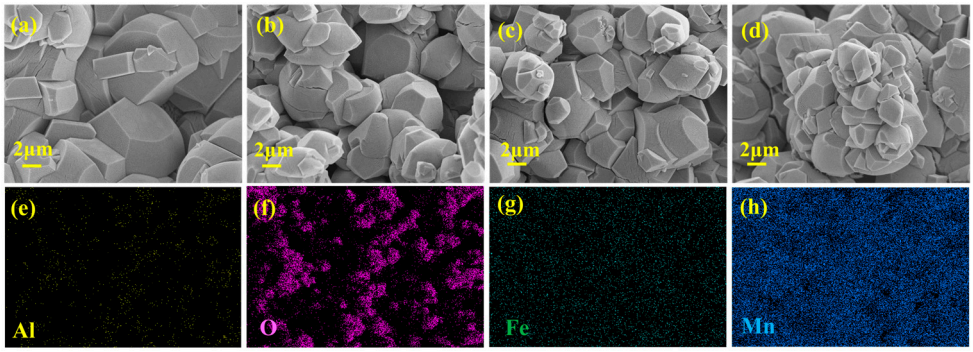

Figure 4. SEM images of Fe_x-Mn_2O_3/γ-Al_2O_3/Al (x = 0, 4.25, 6.61 and 8.32) (**a**–**d**) and EDS mapping images of the $Fe_{6.61}$-Mn_2O_3/γ-Al_2O_3/Al catalyst (**e**–**h**).

In addition, Figure 4e,f shows the EDS mapping images of the $Fe_{6.61}$-Mn_2O_3/γ-Al_2O_3/Al catalyst. The atomic percentages of Al, O, Fe, and Mn on the catalyst surface are 0.30%, 39.12%, 0.45%, and 60.13%, respectively. These results indicate that manganese oxides dominate the catalyst surface. The Fe content is relatively low. This suggests that Fe species are mainly covered by Mn species. Therefore, Mn_2O_3 serves as the main active site of the catalyst, while Fe mainly acts as a promoter.

To clarify the influence of Fe doping on catalytic behavior, the NH_3-SCO performance of the catalysts was further investigated. As shown in Figure 5a–c, the NH_3 conversion, N_2 selectivity, and N_2 yield were systematically evaluated under varying temperature conditions. The results indicated that the introduction of different Fe loadings into Mn_2O_3/γ-Al_2O_3/Al significantly enhanced NH_3 conversion in the 100–240 °C range. Among the catalysts, $Fe_{6.61}$-Mn_2O_3/γ-Al_2O_3/Al exhibited the best performance, achieving complete NH_3 conversion at 210 °C. Furthermore, $Fe_{6.61}$-Mn_2O_3/γ-Al_2O_3/Al maintained N_2 selectivity above 75% in the 200–300 °C range, indicating that Fe doping effectively improved NH_3 conversion without adversely affecting product distribution. Considering both NH_3 conversion and N_2 selectivity, the $Fe_{6.61}$-Mn_2O_3/γ-Al_2O_3/Al catalyst demonstrated superior overall NH_3-SCO performance.

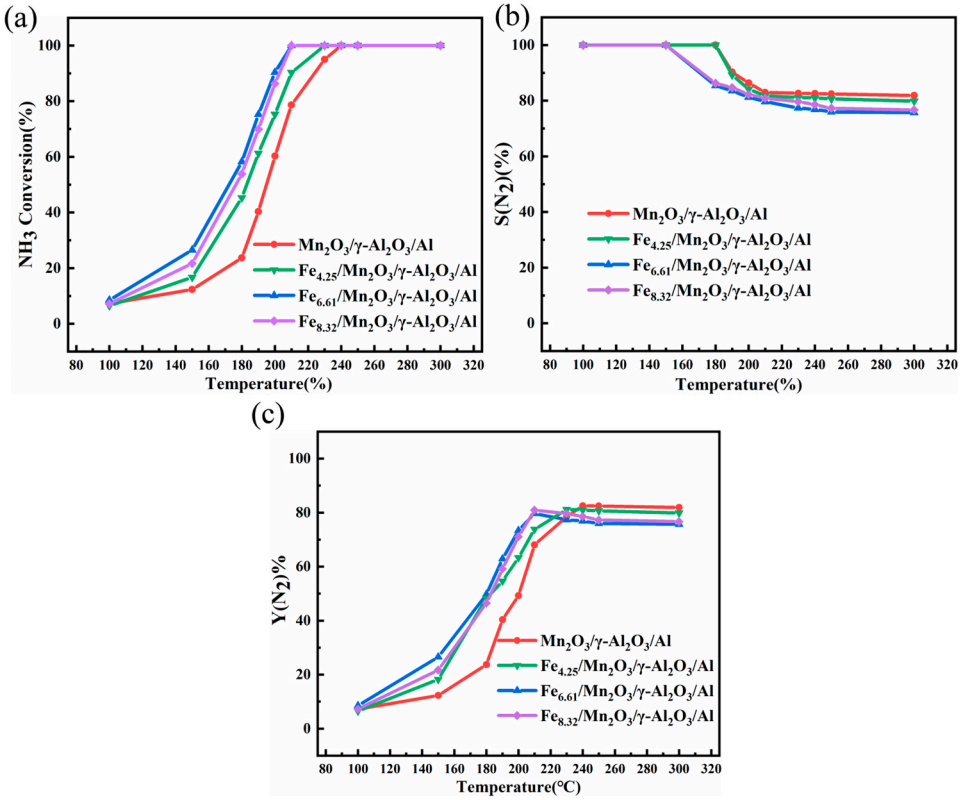

Figure 5. NH_3 conversion (**a**), N_2 selectivity (**b**) and N_2 yield (**c**) of Fe_x-Mn_2O_3/γ-Al_2O_3/Al (x = 0, 4.25, 6.61 and 8.32) catalysts (reaction conditions: [NH_3] = 3000 ppm; WHSV = 25,000 mL·g_{cat}^{-1}·h^{-1}).

In addition, XPS was used to assess the surface valence states and chemical composition of the catalysts. The Mn 2p spectrum showed peaks at 641.0 eV and 642.5 eV, corresponding to Mn^{3+} and Mn^{4+} [29], with the catalyst predominantly existing as Mn_2O_3 and Mn^{3+} as the major valence state, consistent with XRD. A low AOS typically indicates a higher Mn^{3+} content [30,31]. The Jahn–Teller effect of Mn^{3+} ions [32] causes distortion of the Mn-O octahedra, activating lattice oxygen and generating reactive oxygen species (O^-, O_2^{2-}, or surface-adsorbed oxygen), thereby facilitating oxidation [12,33].

The O1s spectrum (Figure 6a) showed two peaks: O_{ads} (531.2–531.5 eV) and O_{latt} (529.7–529.8 eV) [34]. O_{ads} serves as an indicator of oxygen vacancy content and plays a more significant role in catalytic activity due to its higher mobility and oxidative potential [35]. The O_{ads}/O_{latt} ratio follows the order: $Fe_{6.61}$-Mn_2O_3/γ-Al_2O_3/Al > $Fe_{8.32}$-Mn_2O_3/γ-Al_2O_3/Al > $Fe_{4.25}$-Mn_2O_3/γ-Al_2O_3/Al > Mn_2O_3/γ-Al_2O_3/Al, indicating that $Fe_{6.61}$-Mn_2O_3/γ-Al_2O_3/Al adsorbs and activates oxygen more efficiently [36]. The results agree with the SEM observations. The SEM images of $Fe_{6.61}$-Mn_2O_3/γ-Al_2O_3/Al (Figure 4c) show a more uniform particle size distribution and smaller grains. Mn_2O_3 particles are well exposed on the surface, which facilitates the adsorption of active oxygen species.

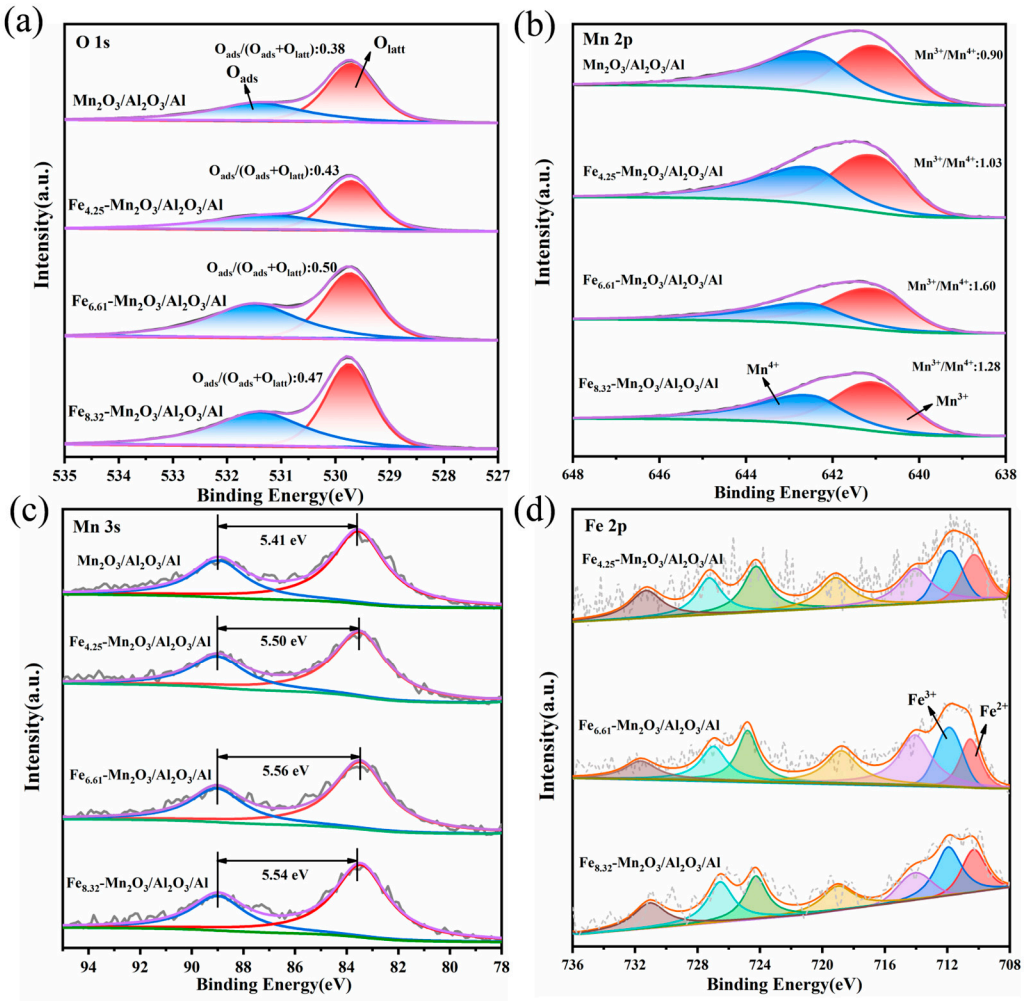

Figure 6. XPS results of Fe_x-Mn_2O_3/γ-Al_2O_3/Al (x = 0, 4.25, 6.61 and 8.32) catalysts: O 1s (**a**), Mn 2p (**b**), Mn 3s (**c**), and Fe 2p (**d**).

The Fe 2p spectrum of $Fe_{6.61}$-Mn_2O_3/γ-Al_2O_3/Al (Figure 6d) displayed peaks at 724.8 eV and 710.5 eV, corresponding to Fe $2p_{1/2}$ and Fe $2p_{3/2}$, and satellite peaks at 718.8 eV and 731.6 eV confirmed Fe^{3+} presence [35,37]. Fitting of the Fe $2p_{3/2}$ main peak showed Fe^{2+} (710.5 eV) and Fe^{3+} (711.9 eV), indicating a mixed Fe^{3+}/Fe^{2+} valence state on the surface [37]. The Fe^{3+}/Fe^{2+} ratios for the Fe_x-Mn_2O_3/γ-Al_2O_3/Al samples were 1.11, 1.42, and 1.39 (Table 3). It was observed that a higher Fe^{3+}/Fe^{2+} ratio was generally accompanied by improved NH_3 catalytic activity. This enhancement may be attributed to increased surface Fe^{3+} species facilitating NH_3 dehydrogenation [38,39] and thus boosting the NH_3-SCO performance.

Table 3. XPS fitting of the O 1s, Mn 2p, Mn 3s, and Fe 2p peaks.

Catalyst	Mn^{4+}(eV)	Mn^{3+}(eV)	O_{ads}(eV)	O_{latt}(eV)	$O_{ads}/(O_{ads}+O_{latt})$	Mn^{3+}/Mn^{4+}	AOS	Fe^{3+}/Fe^{2+}
Mn_2O_3/γ-Al_2O_3/Al	642.4	641.0	531.4	529.7	0.38	0.90	2.86	/
$Fe_{4.25}$-Mn_2O_3/γ-Al_2O_3/Al	642.5	641.0	531.2	529.7	0.43	1.03	2.72	1.11
$Fe_{6.61}$-Mn_2O_3/γ-Al_2O_3/Al	642.5	641.1	531.5	529.7	0.50	1.60	2.76	1.42
$Fe_{8.32}$-Mn_2O_3/γ-Al_2O_3/Al	642.5	641.0	531.4	529.8	0.47	1.28	2.70	1.39

Furthermore, although the Fe loading is relatively high (4.25–8.32 wt%), the Fe 2p signal intensity in the XPS spectra is much weaker than that of Mn. This observation suggests that Fe species are mainly located beneath the Mn layer rather than being enriched on the catalyst surface. Consequently, the catalyst surface is dominated by Mn species, which is consistent with the EDS results.

The redox properties of the catalysts were evaluated using H_2-TPR, as shown in Figure 7a. Two reduction processes were observed for all catalysts: the transformation from Mn_2O_3 to Mn_3O_4 and from Mn_3O_4 to MnO [12]. Mn_2O_3/γ-Al_2O_3/Al showed peaks at 382 °C and 478 °C, $Fe_{4.25}$-Mn_2O_3/γ-Al_2O_3/Al at 369 °C and 474 °C, $Fe_{6.61}$-Mn_2O_3/γ-Al_2O_3/Al at 354 °C and 460 °C, and $Fe_{8.32}$-Mn_2O_3/γ-Al_2O_3/Al at 358 °C and 462 °C. Compared to Mn_2O_3/γ-Al_2O_3/Al, Fe doping shifts both peaks to lower temperatures. As Fe loading increases, the reduction peak temperatures first decrease, then slightly increase. The reduction temperature correlates with catalytic performance: lower reduction temperatures typically result in higher activity [40]. The order of reduction temperatures is: Mn_2O_3/γ-Al_2O_3/Al > $Fe_{4.25}$-Mn_2O_3/γ-Al_2O_3/Al > $Fe_{8.32}$-Mn_2O_3/γ-Al_2O_3/Al > $Fe_{6.61}$-Mn_2O_3/γ-Al_2O_3/Al, indicating that $Fe_{6.61}$-Mn_2O_3/γ-Al_2O_3/Al has stronger reducibility at low temperatures. Additionally, $Fe_{6.61}$-Mn_2O_3/γ-Al_2O_3/Al exhibits a larger reduction peak area, suggesting a higher concentration of active oxygen species [41].

O_2-TPD was used to investigate the amount and binding strength of surface active oxygen species on the catalysts. It was known that oxygen species desorbed below 300 °C are typically associated with highly mobile surface-adsorbed oxygen [42,43], while peaks in the 300–600 °C range correspond to the release of lattice oxygen [43]. Since the NH_3-SCO reaction occurs in the 100–300 °C range, the low-temperature desorption peaks reflect the catalyst's oxygen supply capability under reaction conditions. As shown in Figure 7b, $Fe_{6.61}$-Mn_2O_3/γ-Al_2O_3/Al shows the largest low-temperature peak area, indicating a higher proportion of weakly bound active oxygen. Fe doping enhances O_2 activation and dissociation, leading to increased active oxygen species and better oxygen migration. Increasing Fe loading from 0 to 6.61 wt% significantly boosts desorbed oxygen species. However, at 8.32 wt%, excess Fe may form aggregates or compete with Mn-O-Mn bonds, reducing oxygen vacancy formation and slightly lowering desorbed oxygen species compared to $Fe_{6.61}$-Mn_2O_3/γ-Al_2O_3/Al. This trend aligns with the O_{ads}/O_{latt} ratio from XPS, where $Fe_{6.61}$-Mn_2O_3/γ-Al_2O_3/Al shows the highest O_{ads} ratio, confirming the O_2-TPD results.

As shown in Figure 7c, the variation in O_{ads}/O_{total} closely correlates with the redox properties of the samples: catalysts with a higher proportion of surface-adsorbed oxygen exhibit stronger oxygen mobility and redox ability, as indicated by a lower T_{90} (the temperature at which NH_3 conversion reaches 90%) and enhanced NH_3-SCO activity.

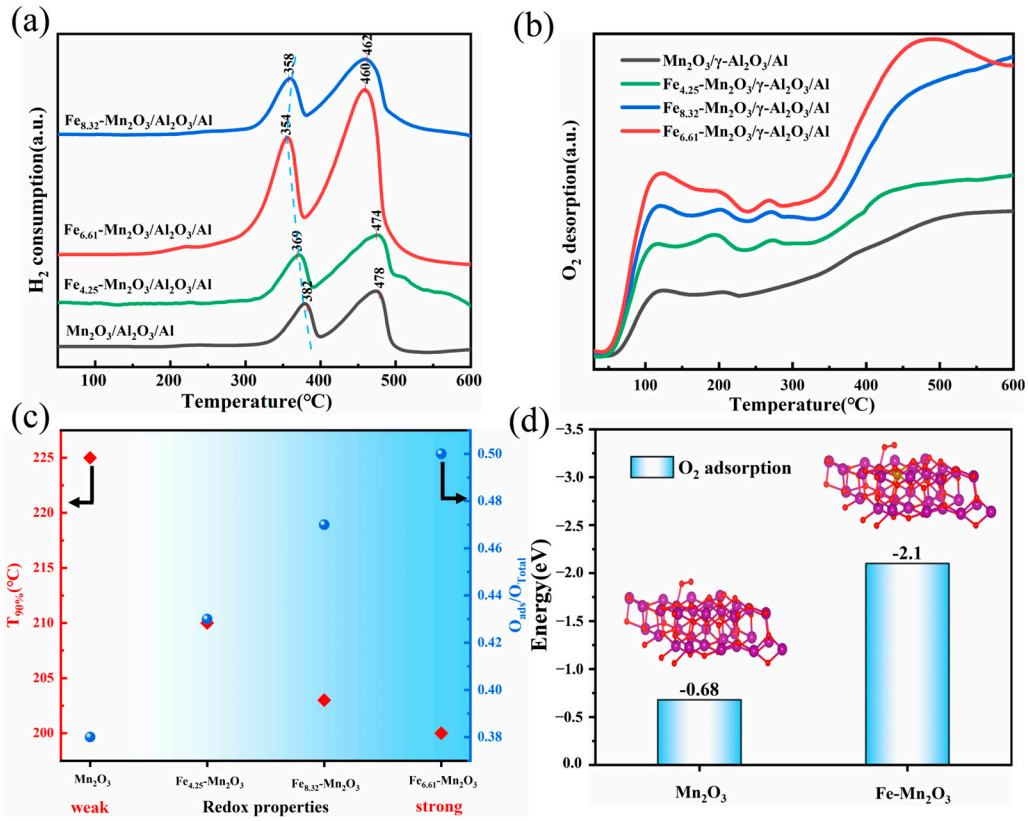

Figure 7. H_2-TPR (**a**) and O_2-TPD (**b**) profiles of Fe_x-Mn_2O_3/γ-Al_2O_3/Al (x = 0, 4.25, 6.61 and 8.32) catalysts. Results for the relationship between T_{90}, redox properties and O_{ads}/O_{total} for different catalysts (**c**). Adsorption models and adsorption energy profiles of O_2 on Mn_2O_3(222) and Fe-Mn_2O_3 sites (**d**).

To investigate the enhancement of oxygen activation in Mn_2O_3 by Fe doping in NH_3-SCO, an analysis from an electronic structure perspective was performed. DFT calculations revealed that the O_2 adsorption energy of Fe-Mn_2O_3 is −2.10 eV, whereas for undoped Mn_2O_3(222) it is only −0.68 eV (Figure 7d). The more negative adsorption energy suggests that the Fe-doped system forms stronger chemisorption with O_2, thereby promoting oxygen activation and dissociation on the catalyst surface.

Therefore, it is reasonable to conclude that a higher proportion of surface-adsorbed oxygen species, in conjunction with its superior redox properties, plays a key role in endowing the $Fe_{6.61}$-Mn_2O_3/γ-Al_2O_3/Al catalyst with excellent NH_3-SCO activity.

It is well established that surface acidity plays a crucial role in NH_3 adsorption and activation during the NH_3-SCO reaction. Therefore, NH_3-TPD was conducted to investigate the acidic properties of the Fe_x-Mn_2O_3/γ-Al_2O_3/Al catalysts. As shown in Figure 8, Fe incorporation significantly altered the acidic structure. All Fe-doped samples exhibited NH_3 desorption peaks around 200 °C, which are assigned to weak acid sites [44]. The undoped Mn_2O_3/γ-Al_2O_3/Al showed much weaker intensity in this region. In addition, Fe-doped catalysts displayed clear desorption peaks at approximately 350 °C, corresponding to medium-strength acid sites [45]. These peaks were absent in the undoped sample, indicating that Fe doping promotes the formation of medium-strength acid sites. As the Fe loading increased, the intensity of the medium-temperature peaks gradually increased. Among the samples, $Fe_{6.61}$-Mn_2O_3/γ-Al_2O_3/Al exhibited the strongest medium-strength acidity, which may account for its superior NH_3-SCO performance.

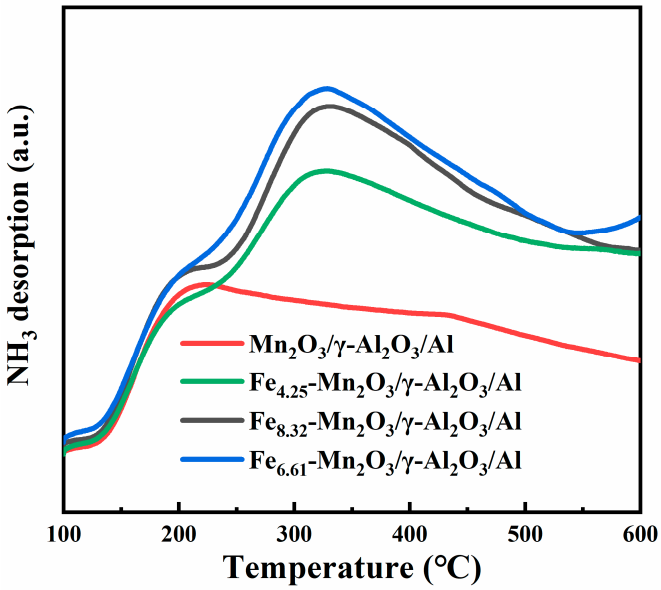

Figure 8. NH_3-TPD profiles of Fe_x-Mn_2O_3/γ-Al_2O_3/Al (x = 0, 4.25, 6.61 and 8.32) catalysts.

To further clarify the intrinsic effect of Fe doping on reaction kinetics, kinetic analysis was carried out over Mn_2O_3/γ-Al_2O_3/Al and $Fe_{6.61}$-Mn_2O_3/γ-Al_2O_3/Al catalysts. To eliminate diffusion effects, 1 g of catalyst was mixed and diluted with 5 g of quartz sand of the same particle size, and the catalytic tests were conducted at a space velocity of 165,000 $mL \cdot g_{cat}^{-1} \cdot h^{-1}$. Under these conditions, the NH_3 conversion was maintained below 15%, satisfying the criteria for excluding internal and external diffusion limitations. The reaction rate (r) and apparent activation energy (E_a) were calculated according to Equations (1)–(3):

$$f_{NH_3}(mol \cdot h^{-1}) = \frac{Q_{NH_3}(m^3 \cdot h^{-1})}{V_m(m^3 \cdot mol^{-1})} \quad (1)$$

$$r\ (mol \cdot g^{-1} \cdot h^{-1}) = \frac{X_{NH_3}\ (vol\%) \times f_{NH_3}(mol \cdot h^{-1})}{m_{cat}\ (g)} \quad (2)$$

$$\ln r = -\frac{E_a}{R \times T} + \ln A \quad (3)$$

As shown in Figure 9, the apparent activation energy (Ea) for the Mn_2O_3/γ-Al_2O_3/Al catalyst was 58.03 $kJ \cdot mol^{-1}$, while for the Fe-modified $Fe_{6.61}$-Mn_2O_3/γ-Al_2O_3/Al catalyst, Ea decreased to 42.11 $kJ \cdot mol^{-1}$. The lower activation energy accelerates the NH_3 oxidation reaction at lower temperatures, further confirming that Fe modification enhances reaction efficiency by reducing the reaction energy barrier.

2.3. Effect of Fe Modification on the H_2O and SO_2 Resistance Behavior of the Catalyst

Industrial flue gas typically contains complex components, among which H_2O and SO_2 are two major impurities. Therefore, evaluating the tolerance of catalysts toward H_2O and SO_2 is essential. Firstly, the water resistance of Mn_2O_3/γ-Al_2O_3/Al and $Fe_{6.61}$-Mn_2O_3/γ-Al_2O_3/Al was evaluated at their respective temperatures for complete NH_3 conversion. As shown in Figure 10a, after introducing 10 vol.% H_2O, the NH_3 conversion gradually decreased and then stabilized. The steady-state conversion was 65% for Mn_2O_3/γ-Al_2O_3/Al and 80% for $Fe_{6.61}$-Mn_2O_3/γ-Al_2O_3/Al. This decline is mainly attributed to the competitive adsorption of H_2O and NH_3 on active sites [46]. After H_2O was removed from the feed, both catalysts recovered their activity. The NH_3 conversion over Mn_2O_3/γ-Al_2O_3/Al returned to 100% within 40 min. In contrast, $Fe_{6.61}$-Mn_2O_3/γ-Al_2O_3/Al recovered to full conversion within 20 min.

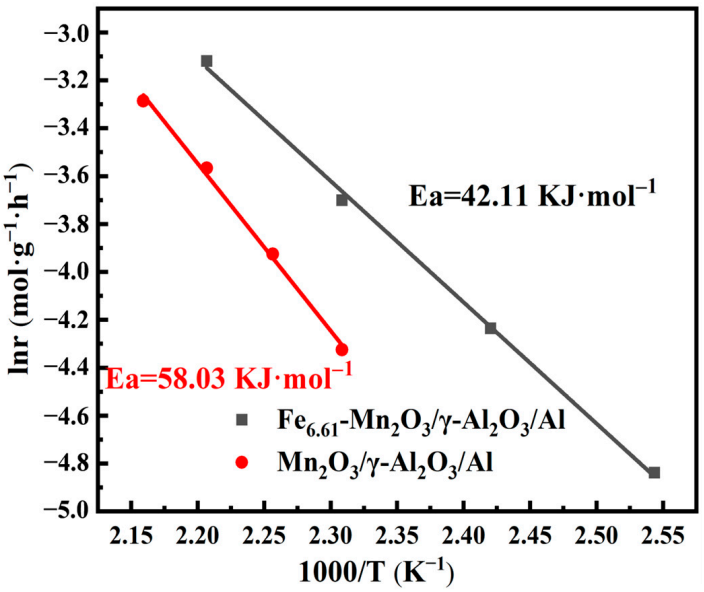

Figure 9. Arrhenius linear regression curves of $Mn_2O_3/\gamma\text{-}Al_2O_3/Al$ and $Fe_{6.61}\text{-}Mn_2O_3/\gamma\text{-}Al_2O_3/Al$ (reaction conditions: 1 g catalyst, weight hourly space velocity (WHSV) = 165,000 $mL{\cdot}g_{cat}^{-1}{\cdot}h^{-1}$, 1000 ppm NH_3 mixed in air).

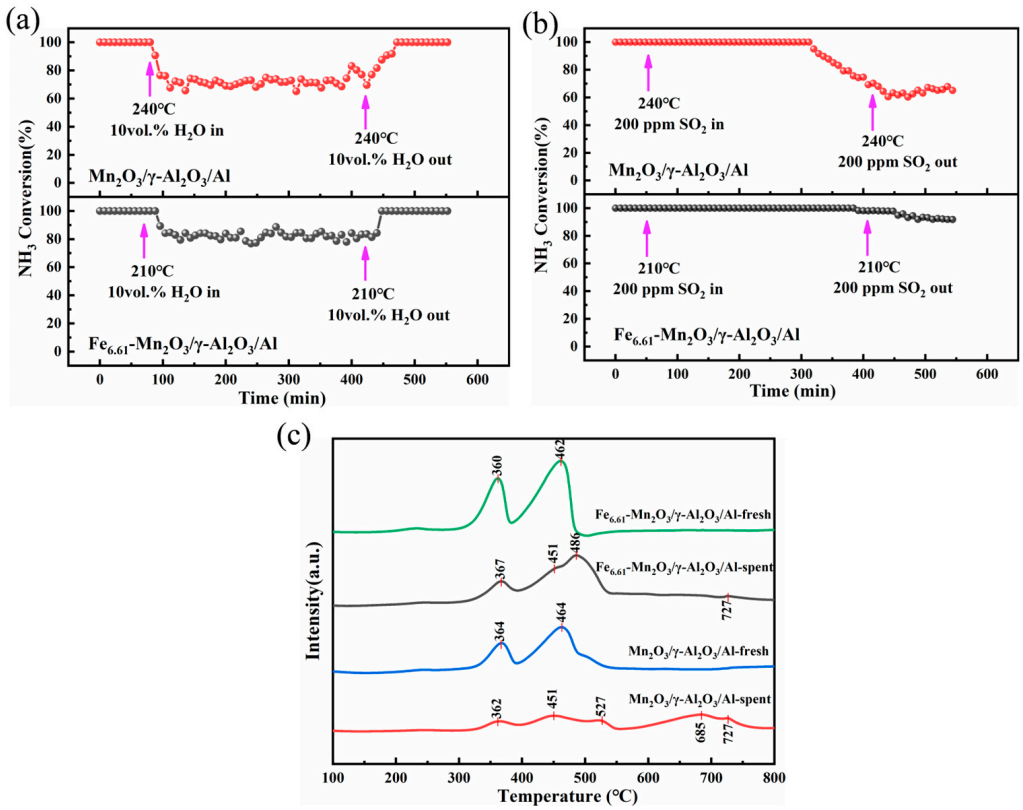

Figure 10. H_2O tolerance (**a**), SO_2 tolerance (**b**), and H_2-TPR profiles (**c**) (before and after sulfur resistance reaction) of $Mn_2O_3/\gamma\text{-}Al_2O_3/Al$ and $Fe_{6.61}\text{-}Mn_2O_3/\gamma\text{-}Al_2O_3/Al$ (reaction conditions: 3000 ppm NH_3; 200 ppm SO_2 (when used), 10.0 vol.% H_2O (when used), and WHSV = 25,000 $mL{\cdot}g_{cat}^{-1}{\cdot}h^{-1}$).

Secondly, as shown in Figure 10b, the sulfur resistance of $Mn_2O_3/\gamma\text{-}Al_2O_3/Al$ and $Fe_{6.61}\text{-}Mn_2O_3/\gamma\text{-}Al_2O_3/Al$ was evaluated at their respective temperatures for complete NH_3 conversion. For $Mn_2O_3/\gamma\text{-}Al_2O_3/Al$, NH_3-SCO activity was stable at 100% conversion with 200 ppm SO_2, but after 260 min of SO_2 exposure, deactivation occurred, and the conversion dropped to 67% after 360 min. No recovery was observed after SO_2 removal,

mainly due to sulfation of active sites and ammonium sulfate deposition [47]. In contrast, $Fe_{6.61}$-Mn_2O_3/γ-Al_2O_3/Al showed enhanced SO_2 tolerance, maintaining complete NH_3 conversion for 320 min under 200 ppm SO_2. After 360 min, the conversion remained above 98%. After SO_2 removal, conversion decreased to 92% and stabilized. Figure 10c shows H_2-TPR profiles of both catalysts before and after SO_2 exposure. For Mn_2O_3/γ-Al_2O_3/Al, after the SO_2 reaction, low-temperature reduction peaks (364 °C and 464 °C) decreased significantly, and new peaks appeared at 685 °C and 717 °C, indicating the formation of inert sulfate species [48], In contrast, $Fe_{6.61}$-Mn_2O_3/γ-Al_2O_3/Al maintained the low-temperature reduction peak (367 °C), with weak high-temperature sulfate reduction peaks, demonstrating that Fe doping effectively suppresses sulfation poisoning.

2.4. Reaction Mechanism of NH_3-SCO over Fe-Mn_2O_3

To reveal the reaction mechanism, in situ FTIR spectroscopy was systematically employed to observe NH_3 adsorption behavior and the dynamic evolution of surface intermediates on Fe-Mn_2O_3 catalysts between 50 and 300 °C. As shown in Figure 11a, absorption peaks at 1087, 1162, 1210–1212, and 1235–1245 cm^{-1} correspond to NH_3 adsorbed on Lewis acid sites (LA) [49–51], while the characteristic peaks at 1357 and 1367 cm^{-1} can be attributed to NH_4^+ on Brønsted acid (BA) sites [52]. As the temperature increases, the intensity of the NH_3/NH_4^+-related peaks gradually strengthens, indicating that the Fe-Mn_2O_3 surface possesses both LA and BA sites and has good NH_3 adsorption and activation abilities. Meanwhile, during the heating process, the formation of nitrate intermediates was clearly observed, including bridging nitrates (1619 cm^{-1}), bidentate nitrates (1557, 1545 cm^{-1}), and monodentate nitrates (1536, 1507, 1453 cm^{-1}) [52–54]. It is widely accepted that nitrate species are key intermediates in the i-SCR pathway [55,56]. Therefore, the above results indicate that the NH_3-SCO reaction on Fe-Mn_2O_3 mainly follows the i-SCR mechanism. Furthermore, the broad peak at 3200–3500 cm^{-1} can be assigned to N-H stretching vibrations (NH_3, NH_4^+, -NH_2, and -NH) [52,53], and its intensity significantly increases with temperature, suggesting that the adsorbed NH_3 and NH_4^+ species are gradually converted to -NH_x species and nitrate intermediates with the involvement of the catalyst's lattice oxygen [55].

To further elucidate the role of oxygen during the reaction, Fe-Mn_2O_3 was pre-adsorbed with NH_3 for 30 min at 300 °C, followed by the introduction of 10 vol.% O_2, and the evolution of surface species is shown in Figure 11b. It can be observed that the peak intensity of bridging nitrates (1619 cm^{-1}) and bidentate and monodentate nitrates (1557–1507 cm^{-1}) remained stable during the entire O_2 introduction process, without significant accumulation. Meanwhile, the LA-NH_3 (1235, 1086 cm^{-1}), BA-NH_4^+ (1367 cm^{-1}), monodentate nitrate (1453 cm^{-1}), and N-H vibration peaks at 3100–3500 cm^{-1} gradually weakened with the introduction of O_2. Notably, the characteristic peak of -NH species (1463 cm^{-1}) [50], which appeared during NH_3 pre-adsorption, also gradually diminished and eventually disappeared as the reaction progressed.

These results indicate that the -NH_x species on the Fe-Mn_2O_3 surface continue to participate in the reaction and are gradually consumed in the O_2 atmosphere. However, their consumption does not lead to significant accumulation of nitrate intermediates. This suggests that once nitrate species are formed, they can rapidly react with the adjacent -NH_x species and be converted into N_2, following the i-SCR reaction pathway (-NH_x + NO_x^- → N_2). This process forms a relatively balanced and mild redox cycle on Fe-Mn_2O_3, effectively preventing excessive accumulation of nitrate and high-valent nitrogen oxides, thus explaining its high N_2 selectivity and suppression of N_2O by-products.

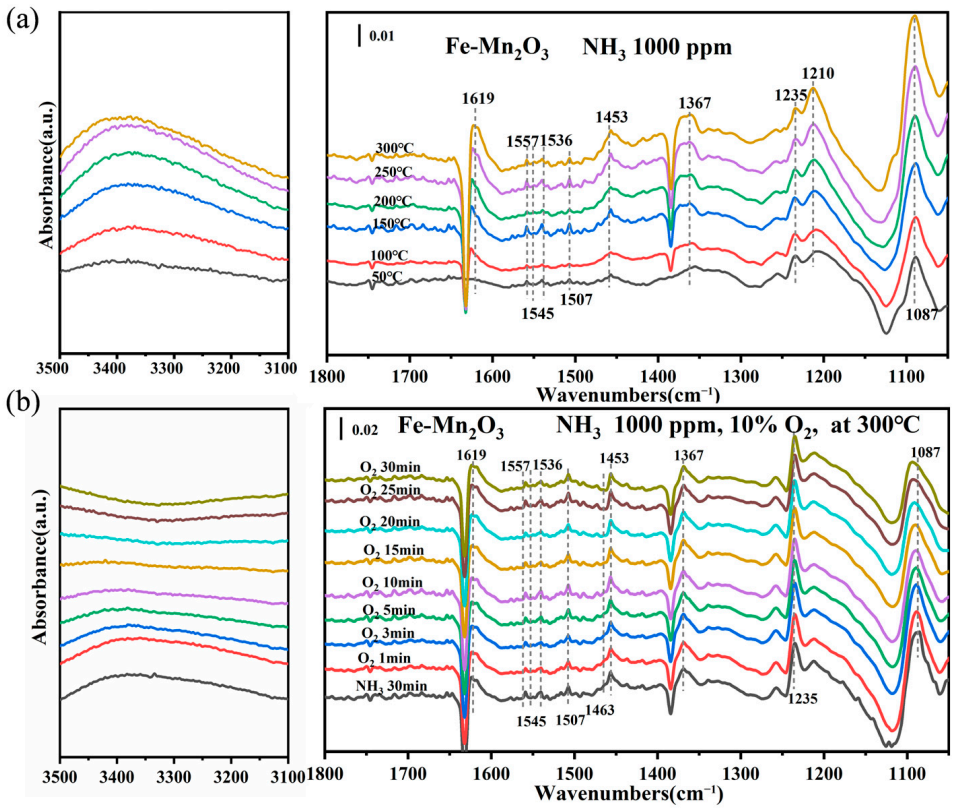

Figure 11. In situ FTIR spectra of NH_3 adsorption over Fe-Mn_2O_3 catalyst at different temperatures (**a**); in situ FTIR spectra of the reaction between O_2 and pre-adsorbed NH_3 over Fe-Mn_2O_3 catalyst at 300 °C (**b**).

Based on the above in situ FTIR results, the following reaction pathway can be reasonably deduced for the NH_3-SCO reaction on Mn-based catalysts (Figure 12): First, NH_3 molecules are adsorbed on the Lewis acid and Brønsted acid sites as NH_3 and NH_4^+, respectively. Then, with the participation of surface active oxygen species, the adsorbed NH_3/NH_4^+ species are gradually dehydrogenated and oxidized to form -NH_2 and -NH intermediates (Equations (4)–(6)). During this process, some -NH_2 species are further oxidized by gaseous O_2 or highly active surface oxygen species, generating surface NO_x species (mainly in the form of NO_2^-/NO_3^-) (Equation (7)). The formed surface NO_x species can couple with adjacent -NH species and be reduced through the i-SCR pathway, ultimately forming N_2 (Equation (8)). However, when the supply of surface -NH species is insufficient or overly oxidized, some NO_x species will not be fully reduced, and their reduction process will remain in the intermediate oxidation state, leading to the formation of N_2O by-products through incomplete reduction (Equation (9)).

$$NH_3 + [O] \rightarrow -NH_2 \quad (4)$$

$$NH_4^+ + [O] \rightarrow -NH_2 \quad (5)$$

$$-NH_2 + [O] \rightarrow -NH \quad (6)$$

$$-NH + [O] \rightarrow -NO_X^- \quad (7)$$

$$-NO_X^- + -NH \rightarrow N_2 + H_2O \quad (8)$$

$$-NO_X^- \rightarrow N_2O \quad (9)$$

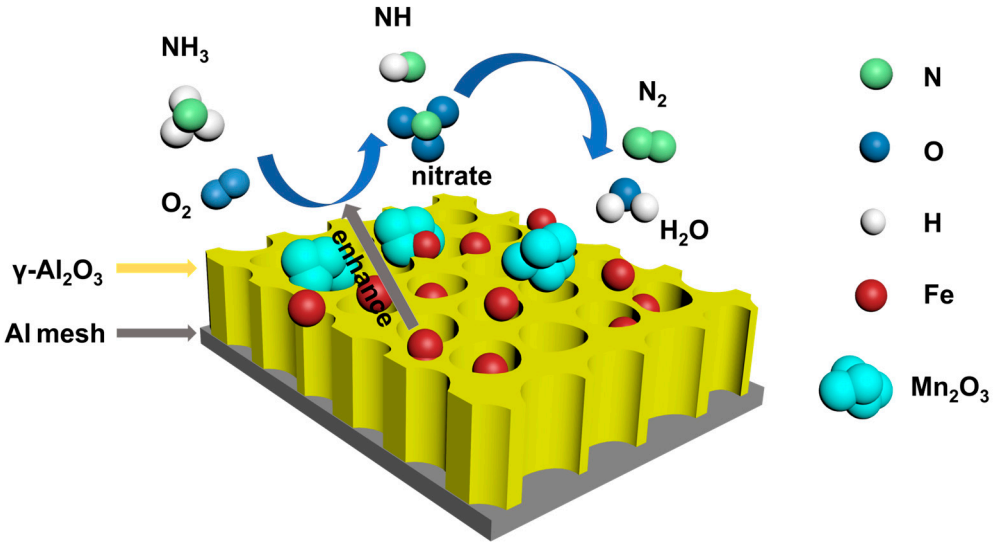

Figure 12. Schematic diagram of the reaction mechanism for NH_3-SCO over Fe-Mn_2O_3/γ-Al_2O_3/Al.

3. Experimental Section

3.1. Catalyst Preparation

Commercial aluminum mesh (1060-type) was used as the substrate. The aluminum mesh was first sequentially treated in 10 wt% NaOH and 10 wt% HNO_3 solutions for several minutes to remove surface grease and impurities. After rinsing with deionized water and drying, the mesh was anodized in an oxalic acid electrolyte under a constant current density of 30 $A \cdot m^{-2}$ for 12 h, resulting in the formation of an ordered anodic aluminum oxide (AAO) film with vertically aligned pore channels. The obtained AAO was calcined at 350 °C for 1 h to remove residual oxalic acid, followed by hydration in deionized water at 80 °C for 1 h [19]. Subsequently, the sample was calcined at 500 °C for 4 h, yielding the mesh-structured γ-Al_2O_3/Al support.

Fe-modified γ-Al_2O_3/Al supports were prepared via an excess impregnation method. Briefly, γ-Al_2O_3/Al was immersed in an aqueous $Fe(NO_3)_3 \cdot 9H_2O$ solution (0.05 $mol \cdot L^{-1}$) for 4–18 h. After impregnation, the samples were thoroughly washed with deionized water, dried under ambient conditions, and calcined at 500 °C for 4 h. The resulting samples were denoted as Fe_x/γ-Al_2O_3/Al, where x represents the Fe loading (wt%), with x = 4.25, 6.61, and 8.32. MnO_2/γ-Al_2O_3/Al and Mn_2O_3/γ-Al_2O_3/Al catalysts were synthesized by a homogeneous precipitation method. Specifically, γ-Al_2O_3/Al was immersed in an aqueous solution containing manganese acetate ($(CH_3COO)_2Mn \cdot 4H_2O$) and urea ($CH_4N_2O$) with a molar ratio of 1:10 and aged for 20 h. After washing with deionized water and drying under ambient conditions, the samples were calcined at 400 °C or 500 °C for 4 h to obtain MnO_2/γ-Al_2O_3/Al and Mn_2O_3/γ-Al_2O_3/Al, respectively. The Fe_x-Mn_2O_3/γ-Al_2O_3/Al catalysts were prepared following the same procedure, except that the γ-Al_2O_3/Al support was replaced by the corresponding Fe_x/γ-Al_2O_3/Al.

3.2. Catalyst Characterization

The morphology of the samples was characterized by field-emission scanning electron microscopy (FESEM, TESCAN MIRA LMS, Brno, Czech Republic). The textural properties were determined by N_2 adsorption–desorption at 77 K using a Micromeritics ASAP 2020-M analyzer (Norcross, GA, USA). Prior to the measurements, all samples were degassed at 350 °C for 12 h, and the specific surface area was calculated by the Brunauer–Emmett–Teller (BET) method. X-ray diffraction (XRD) patterns were recorded on a Bruker (Billerica, MA, USA) D8 Advance diffractometer with Cu Kα radiation, and the data were collected in

the 2θ range of 10–80°. The surface chemical states of the elements were analyzed by X-ray photoelectron spectroscopy (XPS, Thermo Scientific K-Alpha, Waltham, MA, USA), and the binding energies were calibrated using the C 1s peak at 284.8 eV. The reducibility, oxygen mobility, and surface acidity of the catalysts were investigated by H_2 temperature-programmed reduction (H_2-TPR), O_2 temperature-programmed desorption (O_2-TPD), and NH_3 temperature-programmed desorption (NH_3-TPD), respectively, using an AutoChem (Singapore) 2720 chemisorption analyzer. For H_2-TPR, approximately 100 mg of sample was pretreated in a He flow (20 mL·min^{-1}) at 200 °C for 60 min and then cooled to 40 °C. The reduction was carried out from 40 to 600 °C at a heating rate of 10 °C min^{-1} under a 5 vol% H_2/He flow (20 mL·min^{-1}). For O_2-TPD, about 100 mg of sample was pretreated at 80 °C in He (20 mL·min^{-1}) for 60 min and cooled to 40 °C, followed by oxidation under 5 vol% O_2/He (20 mL·min^{-1}) for 30 min. After purging with He (30 mL·min^{-1}) for 1 h, desorption was performed from 40 to 600 °C at a heating rate of 10 °C min^{-1}. The NH_3-TPD measurements were conducted following a similar procedure, except that NH_3/Ar was used as the adsorbing gas. In situ Fourier transform infrared (FTIR) spectroscopy with modulation excitation spectroscopy (MES) was performed on a Bruker Tensor 27 spectrometer equipped with a mercury–cadmium–telluride (MCT) detector to identify reaction intermediates. The spectra were recorded at a resolution of 4 cm^{-1} with 32 scans.

3.3. Catalytic Activity Evaluation

The NH_3 selective catalytic oxidation (NH_3-SCO) performance of the prepared monolithic catalysts (2.5 g) was evaluated in a continuous-flow fixed-bed reactor. As shown in Figure 13, the catalytic activity evaluation setup consisted of a continuous-flow fixed-bed reaction system. The concentrations of NH_3 in the inlet stream and NH_3, NO, NO_2, and N_2O in the outlet stream were analyzed by an online gas chromatograph (GC6600). The feed gas consisted of 3000 ppm NH_3, air, with Ar as the balance gas. The total flow rate was maintained at 340 mL·min^{-1}, corresponding to a weight hourly space velocity (WHSV) of approximately 25,000 mL·$g_{cat}{}^{-1}$·h^{-1}. The NH_3 conversion, N_2 selectivity, and N_2 yield were calculated according to the following equations:

$$\mathrm{NH_3\ Conversion}(\%) = \frac{\mathrm{NH_{3\ in}} - \mathrm{NH_{3\ out}}}{\mathrm{NH_{3\ in}}} \times 100\% \quad (10)$$

$$\mathrm{N_2\ Selectivity}(\%) = \frac{\mathrm{NH_{3\ in}} - \mathrm{NH_{3\ out}} - \mathrm{NO_{out}} - \mathrm{NO_{2\ out}} - 2 \times \mathrm{N_2O_{out}}}{\mathrm{NH_{3\ in}} - \mathrm{NH_{3\ out}}} \times 100\% \quad (11)$$

$$\mathrm{N_2\ yield}(\%) = \frac{\mathrm{NH_3\ Conversion} \times \mathrm{N_2\ Selectivity}}{100} \quad (12)$$

3.4. DFT Method

First-principles calculations were performed using the Vienna Ab initio Simulation Package (VASP 6.3.2). The exchange–correlation interactions were described by the Perdew–Burke–Ernzerhof (PBE) functional within the generalized gradient approximation (GGA). The projector augmented-wave (PAW) method was employed with a plane-wave cutoff energy of 450 eV. All structures were fully optimized until the residual forces on each atom were less than 0.02 eV Å^{-1} and the total energy convergence criterion reached 1×10^{-5} eV. The Brillouin zone was sampled using a $1 \times 1 \times 1$ Monkhorst-Pack k-point mesh for geometry optimizations. A vacuum layer of 15 Å was introduced to avoid interactions between periodic slabs. To properly describe the strong on-site Coulomb interactions of transition-metal 3d electrons, the DFT+U approach based on the Dudarev scheme was adopted, with effective U values of 3.9 eV for Mn and 4.0 eV for Fe.

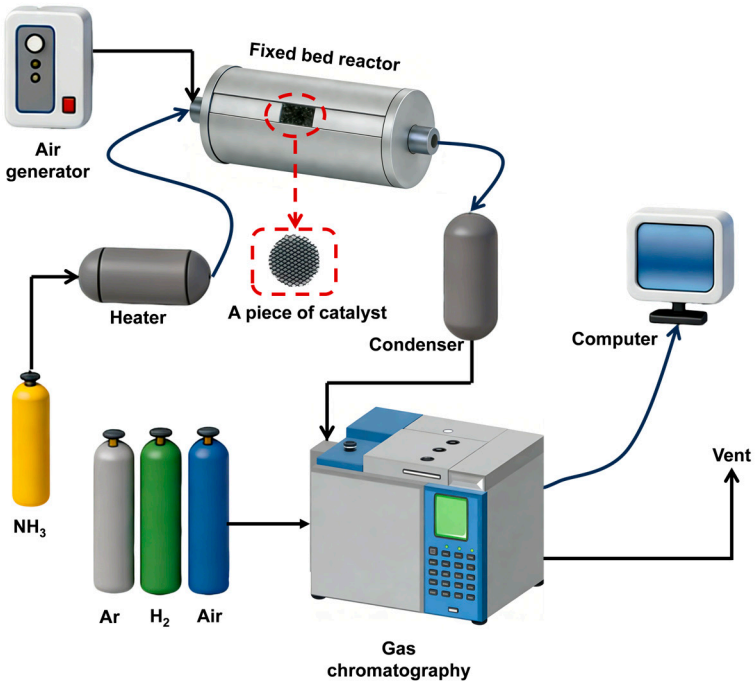

Figure 13. Schematic flowchart of experimental setup for NH_3-SCO reaction.

The adsorption energy of O_2 (E_{ads}) can be defined as:

$$E_{ads} = E_{total} - E_{substrate} - E_{(O\text{-}O)} \quad (13)$$

where E_{total} denotes the total energy of the O_2-adsorbed substrate, and $E_{substrate}$ and $E_{(O\text{-}O)}$ are the energies of the substrate and free O_2, respectively.

4. Conclusions

In this work, a novel structured monolithic Fe-Mn_2O_3/γ-Al_2O_3/Al catalyst was developed to achieve simultaneous high NH_3 conversion and N_2 selectivity at relatively low temperature. The results demonstrate that Fe doping increases the proportion of reactive surface oxygen species (O_{ads}) and strengthens the redox properties of the catalyst, thereby facilitating oxygen activation and effectively improving the catalytic activity toward NH_3 oxidation. DFT calculations further reveal that the introduction of Fe promotes O_2 adsorption on the catalyst surface. Among the catalysts investigated, $Fe_{6.61}$-Mn_2O_3/γ-Al_2O_3/Al achieves complete NH_3 conversion at 210 °C with a high N_2 selectivity of 75%. As shown in Table 4, this performance represents a more favorable balance between low-temperature activity and N_2 selectivity compared with reported Mn-based catalysts. For example, $SmMn_2O_5$ reaches 100% NH_3 conversion at 175 °C but exhibits low N_2 selectivity (45%). $MnMoO_x$ shows relatively high N_2 selectivity (80%) but requires a much higher temperature (340 °C) to achieve 90% NH_3 conversion. In contrast, the present Fe-modified structured catalyst achieves full NH_3 conversion at a relatively low temperature while maintaining improved N_2 selectivity, demonstrating superior overall performance. In addition, the catalyst maintains 92% and 80% of its activity in the presence of 200 ppm SO_2 and 10 vol.% H_2O, respectively. In situ FTIR analysis suggests that the NH_3-SCO reaction over Fe-Mn_2O_3/γ-Al_2O_3/Al predominantly proceeds via the internal selective catalytic reduction (i-SCR) pathway.

Table 4. Comparison of Mn-based catalysts for NH_3-SCO.

Catalysts	Reaction Conditions	Reaction Temperature/°C	NH_3 Conversion/% (N_2 Selectivity/%)	Reference
MnO_2	NH_3 = 1000 ppm; GHSV = 30 L/g·h^{-1}	170	100 (49)	[8]
Mn/Ce-Ti	NH_3 = 50 ppm; GHSV = 40,000 h^{-1}	300	77 (93)	[57]
MnO_x/TiO_2	NH_3 = 500 ppm; 200 mL·min^{-1}	350	93 (80)	[58]
$MnMoO_x$	NH_3 = 500 ppm; 150 mL·min^{-1}	340	90 (80)	[59]
CoMnAl	NH_3 = 5000 ppm; WHSV = 24,000 mL·h^{-1}·g^{-1}	250	100 (40)	[60]
$SmMn_2O_5$	NH_3 = 500 ppm; 200 mL·min^{-1}	175	100 (45)	[61]
$Fe_{6.61}$-Mn_2O_3/γ-Al_2O_3/Al	NH_3 = 3000 ppm; WHSV = 25,000 mL·$g_{cat}$$^{-1}$·h^{-1}	210	100 (75)	This work

Author Contributions: Conceptualization, methodology, writing—original draft preparation, writing—review and editing, J.P.; software, J.P., Q.S., and W.Z.; supervision, project administration, funding acquisition, and review and editing, Q.Z. All authors have read and agreed to the published version of the manuscript.

Funding: This research received no external funding.

Data Availability Statement: The raw data supporting the conclusions of this article will be made available by the authors on request.

Conflicts of Interest: The authors declare no conflicts of interest.

References

1. An, Q.; Xu, G.; Liu, J.; Wang, Y.; Yu, Y.; He, H. Designing a Bifunctional Pt/Cu-SSZ-13 Catalyst for Ammonia-Selective Catalytic Oxidation with Superior Selectivity. *ACS Catal.* **2023**, *13*, 6851–6861. [CrossRef]
2. Wang, X.; Xu, Y.; Zhao, Z.; Liao, J.; Chen, C.; Li, Q. Recent progress of metal-exchanged zeolites for selective catalytic reduction of NO_x with NH_3 in diesel exhaust. *Fuel* **2021**, *305*, 121482. [CrossRef]
3. Zhou, Y.; Jiao, Y.; Lang, J.; Chen, D.; Huang, C.; Wei, P.; Li, S.; Cheng, S. Improved estimation of air pollutant emissions from landing and take off cycles of civil aircraft in China. *Environ. Pollut.* **2019**, *249*, 463–471. [CrossRef]
4. Wang, H.; Lin, M.; Murayama, T.; Feng, S.; Haruta, M.; Miura, H.; Shishido, T. Ag Size/Structure-Dependent Effect on Low-Temperature Selective Catalytic Oxidation of NH_3 over Ag/MnO_2. *ACS Catal.* **2021**, *11*, 8576–8584. [CrossRef]
5. Lan, T.; Zhao, Y.; Deng, J.; Zhang, J.; Shi, L.; Zhang, D. Selective catalytic oxidation of NH_3 over noble metal-based catalysts: State of the art and future prospects. *Catal. Sci. Technol.* **2020**, *10*, 5792–5810. [CrossRef]
6. Liu, J.; Lin, Q.; Liu, S.; Xu, S.; Xu, H.; Chen, Y. Promotional effects of ascorbic acid on the low-temperature catalytic activity of selective catalytic oxidation of ammonia over Pt/SA: Effect of Pt^0 content. *New J. Chem.* **2020**, *44*, 4108–4113. [CrossRef]
7. Lan, T.; Gao, M.; Hasegawa, J.-y.; Shen, Y.; Qu, W.; Hu, Q.; Deng, J.; Cheng, D.; Zhang, D. Isolated Pt Atoms Embedded in CuO Nanocatalysts for Selective Oxidation of Ammonia. *ACS Catal.* **2023**, *13*, 14070–14079. [CrossRef]
8. Qu, Z.; Fan, R.; Wang, Z.; Wang, H.; Miao, L. Selective catalytic oxidation of ammonia to nitrogen over MnO_2 prepared by urea-assisted hydrothermal method. *Appl. Surf. Sci.* **2015**, *351*, 573–579. [CrossRef]
9. Li, G.; Wang, B.; Ma, Z.; Wang, H.; Ma, J.; Zhao, C.; Zhou, J.; Lin, D.; He, F.; Han, Z.; et al. Aluminium-induced component engineering of mesoporous composite materials for low-temperature NH_3-SCR. *Commun. Chem.* **2020**, *3*, 66. [CrossRef]
10. Shu, K.; Guan, B.; Zhu, L.; Zhuang, Z.; Chen, J.; Ma, Z.; Hu, X.; Zhu, C.; Zhao, S.; Dang, H.; et al. A Comprehensive Review of Transition Metal Catalysts in Ammonia Catalytic Oxidation: Recent Advances and Future Perspectives. *Energy Fuels* **2025**, *39*, 15919–15960. [CrossRef]
11. Madhuri, J.V.; Swamy, B.V.; Sudha, M.; Gajula, R.K.; Reddy, P.V.V.; Saha, A. Synergetic Effect of Fe Decorated Mn_2O_3 Support in Application of Aerobic Benzyl Alcohol Oxidation Reaction. *Catal. Surv. Asia* **2025**, *29*, 323–335. [CrossRef]

12. Yu, Y.; Li, F.; Ge, S.; Yang, X.; Rezakazemi, M.; Zang, S.; Aminabhavi, T.M.; Xu, L. Enhanced combustion of toluene on bimetallic-organic frameworks Fe-doped Mn_2O_3 nanoparticles. *Chem. Eng. J.* **2024**, *485*, 149589. [CrossRef]
13. Wu, D.; Song, L.; Zhang, B.; Li, Y. Effect of the mechanical failure of catalyst pellets on the pressure drop of a reactor. *Chem. Eng. Sci.* **2003**, *58*, 3995–4004. [CrossRef]
14. Peng, W.; Yang, Q.; Huang, X.; Fang, Q.; Han, S.; He, J.; Gao, Z. Properties analysis of catalyst particles during stripper distributor fault in industrial fluid catalytic cracking unit. *Fuel* **2025**, *381*, 133279. [CrossRef]
15. Fan, F.; Zhang, Q.; Xu, J.; Ye, Q.; Kameyama, H.; Zhu, Z. Catalytic behavior investigation of a novel anodized Al_2O_3/Al monolith in hydrolysis of dimethyl ether. *Catal. Today* **2013**, *216*, 194–199. [CrossRef]
16. Xie, Z.; Ji, L.; Bian, H.; Zhang, Q. Generation of abundant oxygen vacancies in sandwich structured ε-MnO_2/γ-Al_2O_3/Al by a facile modification strategy for enhanced catalytic decomposition of ozone in humid conditions. *Chem. Eng. J.* **2025**, *509*, 161202. [CrossRef]
17. Cao, M.; Shu, Q.; Zhang, R.; Zhang, Q. Structured Mesh-Type Pt/Mn/γ-Al_2O_3/Al Catalyst Enhanced the CO Oxidation at Room Temperature by In Situ Generation of Hydroxyl: Behavior and Mechanism. *Catalysts* **2025**, *15*, 430. [CrossRef]
18. Xie, Z.; Xia, Q.; Ji, L.; Shu, Q.; Zhang, Q.; Du, P. Ti-modification enhanced the activity of flexible mesh-type Mn/γ-Al_2O_3/Al catalyst for indoor HCHO removal under humid conditions. *Appl. Catal. A Gen.* **2022**, *639*, 118638. [CrossRef]
19. Cao, Z.Y.; Bian, H.R.; Xie, Z.K.; Ji, L.; Zhang, Q. Research and improvement on the performance of Ti modified Mn based catalysts for removing ozone at room temperature. *J. Guizhou Norm. Univ. (Nat. Sci.)* **2024**, *42*, 75–83.
20. Zhang, G.; Zhao, J.; Yang, T.; Zhang, Q.; Zhang, L. In-situ self-assembled Cu_2O/ZnO core-shell catalysts synergistically enhance the durability of methanol steam reforming. *Appl. Catal. A Gen.* **2021**, *616*, 118072. [CrossRef]
21. Xiang, Y.; Liu, H.; Zhang, Q. Numerical Study on Flow Channel Construction of Methanol Steam Reforming Reformer. *Catalysts* **2024**, *14*, 913. [CrossRef]
22. Zhang, Q.; Sun, D.; Fan, F.; Zhang, Q.; Zhu, Z. A novel monolith catalyst of plate-type anodic alumina for the hydrolysis of dimethyl ether. *Catal. Commun.* **2013**, *34*, 64–68. [CrossRef]
23. Xu, S.; Han, Z.; Wu, R.; Cheng, J.; Xu, G. Correlating micro/meso pore evolution and chemical structure variation in a mild thermal treatment of a subbituminite. *RSC Adv.* **2018**, *8*, 9754–9761. [CrossRef]
24. Zhu, Y.; Li, D.; Ji, C.; Si, P.; Liu, X.; Zhang, Y.; Liu, F.; Hua, L.; Han, F. Non-Thermal Plasma Incorporated with Cu-Mn/γ-Al_2O_3 for Mixed Benzene Series VOCs' Degradation. *Catalysts* **2023**, *13*, 695. [CrossRef]
25. Kuwahara, Y.; Fujibayashi, A.; Uehara, H.; Mori, K.; Yamashita, H. Catalytic combustion of diesel soot over Fe and Ag-doped manganese oxides: Role of heteroatoms in the catalytic performances. *Catal. Sci. Technol.* **2018**, *8*, 1905–1914. [CrossRef]
26. Kar, P.; Sardar, S.; Ghosh, S.; Parida, M.R.; Liu, B.; Mohammed, O.F.; Lemmens, P.; Pal, S.K. Nano surface engineering of Mn_2O_3 for potential light-harvesting application. *J. Mater. Chem. C* **2015**, *3*, 8200–8211. [CrossRef]
27. Wei, J.; Zhang, Y.; Sha, H.; Li, Y. Factors influencing the ozone catalytic oxidation of dye wastewater by composite component-supported zeolite. *Surf. Interfaces* **2026**, *87*, 108937. [CrossRef]
28. Han, W.; Yi, H.; Tang, X.; Zhao, S.; Gao, F.; Zhang, X.; Ma, C.; Song, L. Mn-Fe-Ce Coating onto Cordierite Monoliths as Structured Catalysts for NO Catalytic Oxidation. *ChemistrySelect* **2019**, *4*, 4664–4671. [CrossRef]
29. Qiu, J.; Peng, Y.; Tang, M.; Lu, S.; Li, X.; Yan, J. Catalytic activity, selectivity, and stability of co-precipitation synthesized Mn-Ce mixed oxides for the oxidation of 1,2-dichlorobenzene. *Environ. Sci. Pollut. Res. Int.* **2021**, *28*, 65416–65427. [CrossRef] [PubMed]
30. Zhou, Y.; Zhang, H.; Lu, J.; Ran, W.; Rong, S. Surface ammonification regulates oxygen vacancies and acidic sites in δ-MnO_2 to enhance low-temperature selective catalytic oxidation activity of ammonia. *J. Environ. Manag.* **2025**, *380*, 124949. [CrossRef]
31. Meng, S.; Wang, Y.; Wang, B.; Xuan, Y.; Liang, Y.; Zhu, X.; Yun, Y.; Wang, D.; Peng, Y. The strong Fe-Mn interaction over red mud accelerating the activation of key oxygen species for toluene oxidation. *Chem. Eng. J.* **2025**, *509*, 161265. [CrossRef]
32. Hastuti, E.; Subhan, A.; Amonpattaratkit, P.; Zainuri, M.; Suasmoro, S. The effects of Fe-doping on MnO_2: Phase transitions, defect structures and its influence on electrical properties. *RSC Adv.* **2021**, *11*, 7808–7823. [CrossRef]
33. Yang, W.; Zhu, Y.; You, F.; Yan, L.; Ma, Y.; Lu, C.; Gao, P.; Hao, Q.; Li, W. Insights into the surface-defect dependence of molecular oxygen activation over birnessite-type MnO_2. *Appl. Catal. B Environ.* **2018**, *233*, 184–193. [CrossRef]
34. Nie, L.; Li, S.; Chai, S.; Han, N.; Chen, Y. Photothermal catalytic oxidation of toluene with enhanced efficiency over constructed $CuMn_2O_4$/Mn_2O_3 heterojunction catalyst. *Appl. Surf. Sci.* **2022**, *605*, 154567. [CrossRef]
35. Yang, S.; Qi, Z.; Wen, Y.; Wang, X.; Zhang, S.; Li, W.; Li, S. Generation of abundant oxygen vacancies in Fe doped δ-MnO_2 by a facile interfacial synthesis strategy for highly efficient catalysis of VOCs oxidation. *Chem. Eng. J.* **2023**, *452*, 139657. [CrossRef]
36. Bi, F.; Zhang, Y.; Zhou, Z.; Liu, B.; Huang, Y.; Wang, L.; Qin, Y.; Zhang, X. Mn-MIL-100 non-thermally derived MnO_x catalysts for toluene oxidation. *Mater. Lett.* **2024**, *358*, 135888. [CrossRef]
37. Teng, Y.; Wang, X.D.; Liao, J.F.; Li, W.G.; Chen, H.Y.; Dong, Y.J.; Kuang, D.B. Atomically Thin Defect-Rich Fe–Mn–O Hybrid Nanosheets as High Efficient Electrocatalyst for Water Oxidation. *Adv. Funct. Mater.* **2018**, *28*, 1802463. [CrossRef]
38. Ma, S.; Zhao, X.; Li, Y.; Zhang, T.; Yuan, F.; Niu, X.; Zhu, Y. Effect of W on the acidity and redox performance of the $Cu_{0.02}Fe_{0.2}WaTiO_x$ (a = 0.01, 0.02, 0.03) catalysts for NH_3-SCR of NO. *Appl. Catal. B Environ.* **2019**, *248*, 226–238. [CrossRef]

39. Wei, L.; Li, X.; Mu, J.; Wang, X.; Fan, S.; Yin, Z.; Tadé, M.O.; Liu, S. Rationally Tailored Redox Properties of a Mesoporous Mn–Fe Spinel Nanostructure for Boosting Low-Temperature Selective Catalytic Reduction of NO_x with NH_3. *ACS Sustain. Chem. Eng.* **2020**, *8*, 17727–17739. [CrossRef]
40. Han, Z.; Du, Y.; Niu, Z.; Han, P.; Wang, G.; Wang, T.; Li, X.; Shu, J. Cu/Mn co-doped Co_3O_4 with enhanced oxygen activation for low-temperature CO oxidation. *CrystEngComm* **2025**, *27*, 6652–6659. [CrossRef]
41. Wang, Y.; Hu, X.; Li, Y.; Liu, X.; Wang, S.; Wang, C.; Liu, Q.; Liu, B. Ce-doped $La_{2-x}Ce_xCoMnO_6$: Promoting the Co/Mn valence cycle to enhance the catalytic oxidation performance of toluene. *J. Alloys Compd.* **2025**, *1041*, 183714. [CrossRef]
42. Zhang, X.; Zhao, H.; Song, Z.; Liu, W.; Zhao, J.; Ma, Z.a.; Zhao, M.; Xing, Y. Insight into the effect of oxygen species and Mn chemical valence over MnO on the catalytic oxidation of toluene. *Appl. Surf. Sci.* **2019**, *493*, 9–17. [CrossRef]
43. Liu, S.; Zhang, T.; Niu, X.; Zhu, Y. Tunable Mn-O strength in $CuaMnO_x$ (a = 0.06, 0.08, and 0.14): Enhancing toluene and acetone oxidation via simultaneous promotion of adsorbed oxygen content and lattice oxygen mobility. *Sep. Purif. Technol.* **2025**, *379*, 134870. [CrossRef]
44. Chen, C.; Cao, Y.; Liu, S.; Jia, W. The effect of SO_2 on NH_3-SCO and SCR properties over Cu/SCR catalyst. *Appl. Surf. Sci.* **2020**, *507*, 145153. [CrossRef]
45. Zhang, X.; Wang, H.; Jiang, X.; Sun, H.; Qu, Z. Study of synergistic effect between CuO and CeO_2 over CuO@CeO_2 core–shell nanocomposites for NH_3-SCO. *Catal. Sci. Technol.* **2019**, *9*, 2968–2981. [CrossRef]
46. Liu, J.; Zhu, Y.; Sun, Z.; Du, Y.; Xiong, Z.; Zhou, F.; Jin, J.; Yang, Q.; Lu, W. Promotional effect of H_2O introduction on the NH_3-SCR activity of the gas-phase sulfated CeO_2 catalyst by organic CS_2+COS: Influence of H_2O concentration. *J. Environ. Chem. Eng.* **2023**, *11*, 111529. [CrossRef]
47. Yu, Y.; Wei, D.; Tong, Z.; Wang, J.; Chen, J.; He, C. Rationally engineered ReO_x-$CuSO_4/TiO_2$ catalyst with superior NH_3-SCO efficiency and remarkably boosted SO_2 tolerance: Synergy of acid sites and surface adsorbed oxygen. *Chem. Eng. J.* **2022**, *442*, 136356. [CrossRef]
48. Fang, H.; Liang, W.; Ma, L.; Ma, C. Properties and characterization of red mud modified by hydrochloric, sulfuric, and nitric acid for the catalytic oxidation of toluene. *J. Environ. Chem. Eng.* **2023**, *11*, 110943. [CrossRef]
49. Yang, Y.; Wang, M.; Tao, Z.; Liu, Q.; Fei, Z.; Chen, X.; Zhang, Z.; Tang, J.; Cui, M.; Qiao, X. Mesoporous Mn–Ti amorphous oxides: A robust low-temperature NH_3-SCR catalyst. *Catal. Sci. Technol.* **2018**, *8*, 6396–6406. [CrossRef]
50. Lin, M.; An, B.; Niimi, N.; Jikihara, Y.; Nakayama, T.; Honma, T.; Takei, T.; Shishido, T.; Ishida, T.; Haruta, M.; et al. Role of the Acid Site for Selective Catalytic Oxidation of NH_3 over Au/Nb_2O_5. *ACS Catal.* **2019**, *9*, 1753–1756. [CrossRef]
51. Wu, S.; Li, J.; Qiu, J.; Wang, C.; Wang, F.; Li, Z.; Ning, P.; Li, K. Regulating the valence and size of the active center of Co/Al_2O_3 catalyst improved the performance and selectivity of NH_3-SCO. *J. Environ. Sci.* **2025**, *150*, 188–201. [CrossRef]
52. Jabłońska, M.; Beale, A.M.; Nocuń, M.; Palkovits, R. Ag-Cu based catalysts for the selective ammonia oxidation into nitrogen and water vapour. *Appl. Catal. B Environ.* **2018**, *232*, 275–287. [CrossRef]
53. Liu, J.; Li, X.; Zhao, Q.; Ke, J.; Xiao, H.; Lv, X.; Liu, S.; Tadé, M.; Wang, S. Mechanistic investigation of the enhanced NH_3-SCR on cobalt-decorated Ce-Ti mixed oxide: In situ FTIR analysis for structure-activity correlation. *Appl. Catal. B Environ.* **2017**, *200*, 297–308. [CrossRef]
54. Vélez, R.P.; Bentrup, U.; Grünert, W.; Brückner, A. The Role of NO_2 in the Fast NH_3-SCR of NO_x: A Combined In Situ FTIR and EPR Spectroscopic Study. *Top. Catal.* **2017**, *60*, 1641–1652. [CrossRef]
55. Liu, G.; Sun, H.; Wang, H.; Qu, Z. Rational tuning towards B-sites (B = Mn, Co, Al) on CoB_2O_4 binary oxide for efficient selective catalytic oxidation of ammonia. *Chem. Eng. J.* **2023**, *453*, 139941. [CrossRef]
56. Chu, Q.; Wang, X.; Miao, B.; Liu, Y.; Li, Q. Selective catalytic oxidation of NH_3 over Co_3O_4-Cu/KFI composite with superior low-temperature activity and N_2 selectivity. *J. Environ. Chem. Eng.* **2025**, *13*, 116626. [CrossRef]
57. Liu, W.; Long, Y.; Zhou, Y.; Liu, S.; Tong, X.; Yin, Y.; Li, X.; Hu, K.; Hu, J. Excellent low temperature NH_3-SCR and NH_3-SCO performance over Ag-Mn/Ce-Ti catalyst: Evaluation and characterization. *Mol. Catal.* **2022**, *528*, 112510. [CrossRef]
58. Song, D.; Shao, X.; Yuan, M.; Wang, L.; Zhan, W.; Guo, Y.; Guo, Y.; Lu, G. Selective catalytic oxidation of ammonia over MnO_x–TiO_2 mixed oxides. *RSC Adv.* **2016**, *6*, 88117–88125. [CrossRef]
59. Hu, L.; Zhao, Q.; Zhang, X.; Li, H.; Bian, C.; Zeng, Y. Regulating the redox sites of $MMoO_x$ (M = Mn, Fe, Cr) catalysts for highly efficient selective catalytic oxidation of NH_3. *Res. Chem. Intermed.* **2025**, *51*, 4177–4190. [CrossRef]
60. Ludvíková, J.; Jabłońska, M.; Jirátová, K.; Chmielarz, L.; Balabánová, J.; Kovanda, F.; Obalová, L. Co–Mn–Al mixed oxides as catalysts for ammonia oxidation to N_2O. *Res. Chem. Intermed.* **2015**, *42*, 2669–2690. [CrossRef]
61. Chen, Y.; Chen, X.; Ma, X.; Tang, Y.; Zhao, Y.; Zhang, A.; Wang, C.; Du, C.; Shan, B. Selective catalytic oxidation of ammonia over AMn_2O_5 (A = Sm,Y,Gd) and reaction selectivity promotion through Nb decoration. *J. Catal.* **2021**, *402*, 10–21. [CrossRef]